Investigation on the Fracture Mechanism of Self-Healing Mortar Specimens Using Acoustic Emission (AE) Analysis and a Lattice Discrete Element Method (LDEM)

Sci

MDPI

Article

Investigation on the Fracture Mechanism of Self-Healing Mortar Specimens Using Acoustic Emission (AE) Analysis and a Lattice Discrete Element Method (LDEM)

Giuseppe Lacidogna [1,*], Pedro Marin Montanari [1], Boris Nahuel Rojo Tanzi [2], Ignácio Iturrioz [2], Jean-Marc Tulliani [3], Giovanni Anglani [1] and Paola Antonaci [1]

[1] Department of Structural, Geotechnical and Building Engineering, Politecnico di Torino, Corso Duca Degli Abruzzi 24, 10129 Torino, Italy; pedro.marinmontanari@polito.it (P.M.M.); giovanni.anglani@polito.it (G.A.); paola.antonaci@polito.it (P.A.)
[2] Department of Mechanical Engineering, Universidade Federal do Rio Grande do Sul (UFRGS), Rua Sarmento Leite n° 425, Porto Alegre 90050-170, Brazil; boris.rojotanzi@ufrgs.br (B.N.R.T.); ignacio@mecanica.ufrgs.br (I.I.)
[3] Department of Applied Science and Technology, INSTM Research Unit PoliTO-LINCE Laboratory, Politecnico di Torino, Corso Duca degli Abruzzi 24, 10129 Torino, Italy; jeanmarc.tulliani@polito.it
* Correspondence: giuseppe.lacidogna@polito.it

Abstract: This paper discusses the combined application of the Acoustic Emission (AE) technique and a Lattice Discrete Element Method (LDEM) to study the damage process in cement mortar specimens subjected to three-point bending tests. The experimental work was carried out in a previous study by the research team. The specimens contain macro-capsules filled with a polyurethane resin that promotes a self-healing mechanism upon crack formation. The numerical model here developed provides an estimate of the fracture energy of the resin, which is difficult to obtain by relying purely on experimental results. Furthermore, this study includes the analysis of both fracture energy and Acoustic Emission energy based on experimental tests using the same specimens. Through the comparison of experimental and numerical results, a correlation between the toughness of the specimens and AE activity is established. The findings indicate that, for the self-healing specimens, there is a decrease in fracture energy as the emitted Acoustic Emission (AE) energy increases.

Keywords: self-healing cement-based materials; macro-capsules; polyurethane resin; discrete element method; acoustic emission

Academic Editor: Aires Camões

Received: 1 May 2024
Revised: 26 November 2024
Accepted: 12 December 2024
Published: 2 January 2025

Citation: Lacidogna, G.; Montanari, P.M.; Tanzi, B.N.R.; Iturrioz, I.; Tulliani, J.-M.; Anglani, G.; Antonaci, P. Investigation on the Fracture Mechanism of Self-Healing Mortar Specimens Using Acoustic Emission (AE) Analysis and a Lattice Discrete Element Method (LDEM). *Sci* **2025**, *7*, 5. https://doi.org/10.3390/sci7010005

1. Introduction

The study of self-healing concrete and cement-based materials has shown a rapidly increasing trend in recent years due to the practical need to build structures with extended service life that require minimum maintenance [1]. Previous studies have focused on several aspects of this innovative type of material, such as the different options for (intrinsic/stimulated) autogenous healing [2–7] or autonomous healing [8–12]. As indicated in [13], autogenous healing refers to the self-healing capacity intrinsic to concrete, which is achieved naturally through continuing hydration of cement grains, carbonation of calcium hydroxide, physical–mechanical blockage of the crack caused by deposition of impurities and loose particles in the crack flanks, or by expansion of the hydrated concrete matrix. The autogenous healing mechanism can be further improved by incorporating mineral additions, crystalline admixtures, fibers, nanofillers, and internal curing agents (in these cases,

the self-healing mechanism is generally referred to as stimulated autogenous). In contrast, autonomous healing refers to the self-healing capacity provided by the incorporation of unconventional engineered additions, such as capsules containing a healing agent, which is the focus of the present work. The evaluation of the impact of this new class of construction materials from an economic and environmental viewpoint [14–20], and the testing methods to characterize their performances [21–23], have also received great attention from the international scientific community, including the contribution of specialists in Non-Destructive Techniques (NDTs) [24–34]. The fracture energy and crack propagation properties hold substantial significance among the characterization parameters, as they serve as crucial indicators in determining the suitability of a material for a specific application. In this sense, the Acoustic Emission (AE) technique is a good strategy to monitor the damage evolution in quasi-brittle materials. Similarly, AE and other methods based on the propagation of elastic waves into quasi-brittle materials can be effective in monitoring the reverse phenomenon, i.e., the self-healing behavior. This area has gathered significant attention, and studies have been conducted focusing on this aspect with a heavy reliance on experimental findings [24,35,36]. For example, an exhaustive list of references on this topic can be found in [37]. The present study investigates the correlation between AE signals and the fracture energy of self-healing cement mortar specimens subjected to three-point bending tests, based on the substantial analysis of the interaction between AE signals, Kinetic, Elastic, and Dissipated energy during the damage process provided in [38,39].

Relying purely on experimental testing could make it difficult to isolate and understand the contribution of the healing agent in the fracture energy of the tested specimens. Moreover, it would be highly beneficial to have instruments to acquire further insight into the behavior of self-healing cementitious materials and to optimize them without depending only on trial-and-error procedures. In this regard, numerical methods can be very helpful, and are attracting increasing attention from the scientific community interested in the development and characterization of self-healing cementitious materials [40,41]. Traditional computational mechanics analysis usually relies on the finite element method (FEM), which is based on continuous-media hypotheses. This is well fit for material modeling whenever damage can be related to plasticity effects and residual deformations, such as in metal alloys, some classes of polymers, and composite materials. However, for materials where residual deformations are small and damage is governed by energy dissipation, these tools show some limitations. Such is the case of quasi-brittle materials, for example, rocks, ceramics, and concrete. There are additional implementations in the FEM to model these characteristics, such as the cohesive interface method [42] and the extended finite element method (XFEM) [43], among others. In [44,45], the advantages and limitations of these approaches to model the damage process in quasi-brittle materials are discussed. Some applications of such modeling methods to self-healing cementitious materials include but are not limited to [46–48], in which the authors used these types of models to capture the damage-healing behavior of either autogenous or autonomous self-healing cementitious material systems.

On the other hand, discrete element methods (DEMs) could be viewed as an alternative approach, wherein a continuum medium is conceptualized as a network of discrete elements. In this regard, besides the method used in the present work, other viable options are the Peridynamics approach [49–56], the fiber bundle model [57,58], and the fuse model [59–61], among several others which are commonly related to the study of fracture and collapse. Regarding the study of the fracture characteristics in concrete, the use of particle-based methods originally introduced by Cundall and Stack is mentioned in [62]. In the context of self-healing cementitious materials, several discrete methods were used

to model different features of these materials, such as the Lattice Beam Network Model (LBM) [63–66] or the Lattice Discrete Particle Model (LDPM) [67].

In this work, a modified version of the Lattice Discrete Element Method (LDEM), first proposed by Riera in 1984 [68,69], is employed to study the fracture energy of a polymeric resin used as a healing agent in capsule-based self-healing systems, and to analyze the evolution of the fracture surface in self-healing mortar specimens subjected to three-point bending tests. In the LDEM, the continuum is represented by a cubic network consisting of massless uniaxial elements connected to punctual mass elements. The theoretical foundations of this method will be discussed in the subsequent sections, along with the contribution provided by the authors in this field, in some relevant previous studies.

In addition, this study provides a deeper insight into the relationship between the Acoustic Emission energy, as resulting from previous experiments on the same capsule-based self-healing systems [70], and the fracture energy numerically determined through the LDEM.

In this way, the current work contributes to scientific progress in two main aspects. First, it demonstrates the potential of the Lattice Discrete Element Method employed in this study as a tool for simulating the self-healing process of concrete, thereby enhancing our understanding of it. Second, it establishes a correlation between the toughness of the specimens and their AE activity, opening new opportunities for the purposes of monitoring the evolution of self-healing systems.

2. Materials and Methods

2.1. Specimens and Mechanical Tests

The experimental work analyzed in this study was carried out in a previous work by some of the authors [70]. It focused on capsule-based self-healing mortar systems using a polymeric resin as a healing agent. Specifically, the healing agent is a one-component polyurethane (PU) resin produced by Minova CarboTech GmbH Branch Italy (Milan, Italy), Carbostop U [71]. This resin reacts and hardens in contact with moisture from the atmosphere or from the concrete matrix. To avoid unwanted polymerization before testing, the resin was sealed in cementitious tubular macro-capsules measuring 55 mm in length, approx. 5.5 mm in internal diameter, and approx. 8 mm in external diameter. They were manufactured according to previous experiences from the research team [72]. These cementitious capsules have been proved to be effective in encapsulating highly moisture-reactive healing agents [73]. To further protect the healing agent inside the capsule and to avoid any premature hardening, the capsules were coated with a commercial epoxy resin (Plastigel, API SpA, Genova, Italy). The capsules were incorporated (one per specimen) into prismatic beam elements with dimensions 40 mm × 40 mm × 160 mm, made of an ordinary cement mortar mixture. Portland cement (CEM II 42.5 A/LL, Buzzi Unicem SpA, Casale Monferrato, Italy), standard sand (size 0–2 mm), and tap water were used. The ratio of water/cement was up to 0.50, while sand/cement was up to 3. The capsule containing the healing agent was fixed in the center of the mold by means of a nylon thread, about one-third in height, in accordance with [72]. A U-shaped notch was also made in the samples, using a removable plastic piece that was attached to the bottom of the mold. The length of the notch and its height were 4 mm. The mold was filled in two layers and each layer was compacted on a jolting table by 60 jolts. In addition, the mold was covered with plastic sheets until demolding, the day after casting. Finally, the samples were cured in a saturated humidity environment for one week. A specimen and its dimensions can be seen in Figure 1.

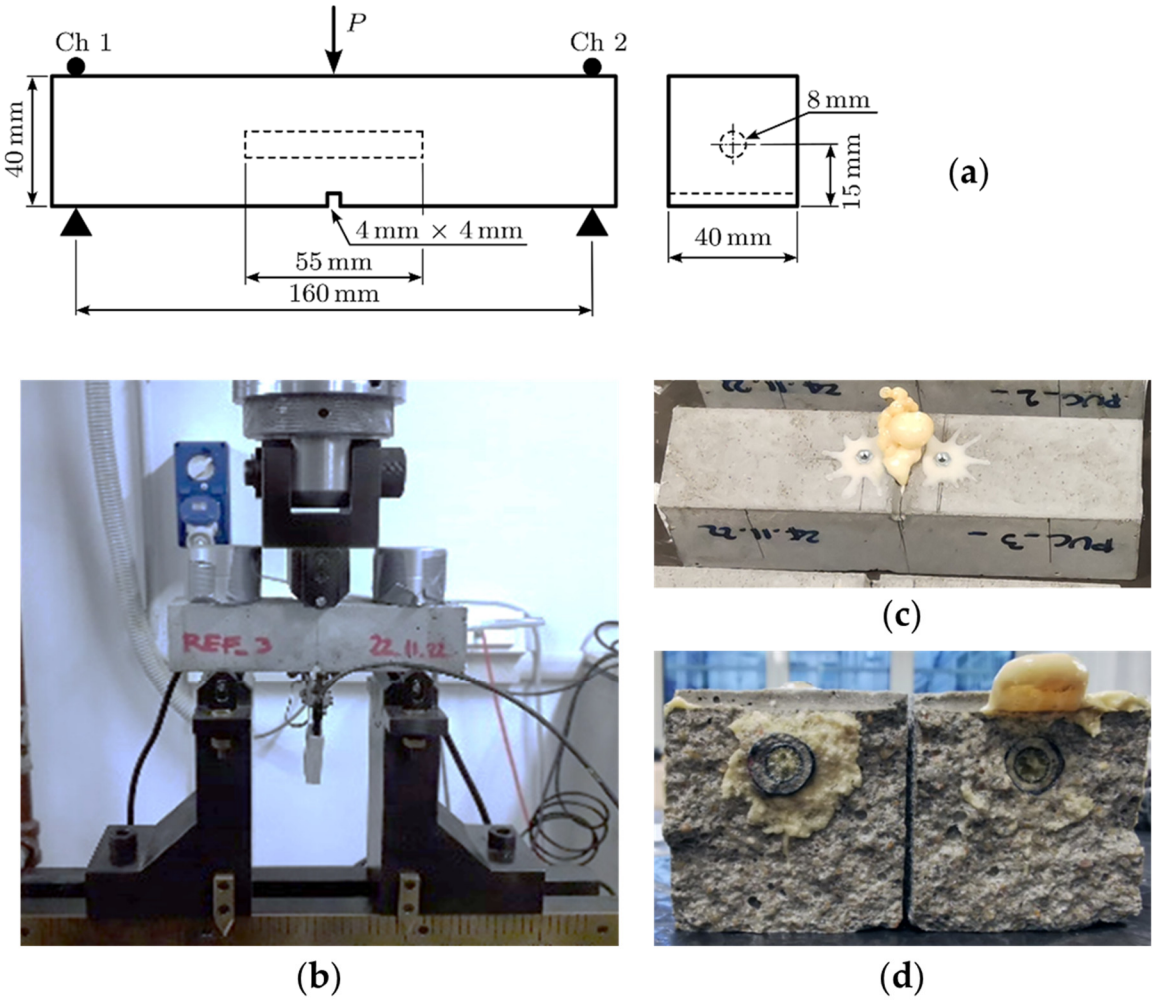

Figure 1. (**a**) Schematic of the testing procedure and the specimen dimensions, (**b**) one of the tests performed in laboratory and, a specimen (**c**) after pre-cracking and (**d**) after a reloading test, where the resin expansion can be clearly observed. Adapted from [70,74], under the terms of the CC BY and CC BY-NC-ND licenses, respectively.

In this study, the test data of three self-healing specimens, before and after the autonomous release of the resin upon cracking, will be discussed.

The mechanical testing was conducted in two parts, each performed using a servo-controlled hydraulic testing machine (MTS) with a maximum load of 250 kN and an accuracy of ±1.0%. This machine has an electronic control mechanism that allows tests to be performed either in load control or displacement control. The tests were performed by simultaneously acquiring AE signals. The first part was performed on the self-healing specimens in their initial (virgin) state and consisted of pre-cracking, i.e., static loading performed by Crack Mouth Opening Displacement (CMOD) control up to a target value of approx. 800 microns under loading. According to the authors' experience, this limit value for the CMOD, considered in the first step of loading, allows the rupture of the cementitious capsules and thus the triggering of the self-healing effect, the same way as it would happen in real structures as a consequence of the formation of medium-large cracks [72]. More details about this point are shown in [70,74].

The device used for CMOD measuring was a DD1 clip gauge manufactured by HBM, which was placed below the specimens across the notch. The mid-span vertical displacement of the specimen was also measured using the vertical stroke of the MTS equipment's piston. This initial mechanical test allowed the creation of a crack at the mid-span of the

specimen, hence activating the capsule breakage and triggering the self-healing mechanism through the autonomous release of the resin contained inside the capsule. The second part was a static reloading. This was performed on specimens once the resin resealed by the capsule upon pre-cracking had hardened, and was carried out under the same conditions as the first pre-cracking test. Figure 1a represents a schematic of the testing procedure, Figure 1b depicts one of the tests performed in laboratory, and Figure 1c,d depict one specimen after the pre-cracking and reloading tests, respectively, where the resin expansion can be clearly observed. For the sake of clarity, in the following, the results of the pre-cracking tests (and/or the related specimens) will be denoted by VI (standing for "virgin"), while the results of the reloading tests (and/or the related specimens) will be referred to as SH (standing for "self-healed").

More details about the experimental campaign carried out are presented in [70,74].

2.2. Acoustic Emission Technique

In the present work, the AE technique is used to obtain information about the damage process in the VI and the SH specimens. This technique consists of capturing internal instabilities in the material core (movements or internal failure) called "events". These perturbations emit elastic waves that arrive at the AE sensors as "signals". Several signals captured by different surface AE devices can be linked to the same event. Using the temporal distribution captured by different AE devices, one could perform the localization of the events in the time and in the spatial domains. Furthermore, the signal information enables the computation of global parameters, providing insights into the potential occurrence of sudden increases in AE activity. This, in turn, can indicate the presence of local instabilities or even the impending collapse of the system. For more extensive details on the AE technique, refer to [37] and other relevant sources. In the present work, the mechanical behavior of the VI and the SH specimens is investigated using AE signals, captured during the experimental tests (Figure 2), and numerical simulations carried out in accordance with the experiments.

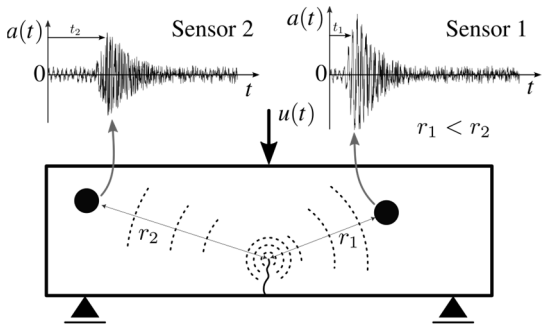

Figure 2. Illustration of an event produced by an internal local instability and the signals captured by the AE sensors on the surface of the material. Note: the figure has illustrative purposes only; the position of the sensors is different from that of the sensors in the experimental tests. It is important to note that the highest signal amplitude occurs when the sensor is close to the location of the event. Adapted from [75], under the terms of the CC BY license.

Regarding AE data acquisition, two Lunitek AEmission sensors were used (model LT18-003-PRD00-R0, Lunitek SrL, Sarzana, Italy) with a frequency range of 15–625 kHz [76]. They were placed on the upper face of the specimens, in correspondence with the supports. The sensors were attached to the specimens with modeling clay. The data acquisition system used a sampling frequency of 5 MHz and stored the data in a parametric format [34]. The parameters recorded for each detected signal were as follows:

- Signal onset time: The time of the first reading beyond the detection limit: 49 dB (280 μV). The amplitude threshold was chosen based on previous experiences in the use of the sensor and acquisition system. In other applications carried out by the research team with the same AE system, the same threshold was used, see for example [34].
- Peak amplitude, expressed in dB, A = 20 $\log_{10}$(V), with V being the amplitude of the AE signal in μV.
- Number of oscillations (counts): Number of intermediate crossings of the 49 dB threshold by the signal. It is also used to estimate the average frequency (AF) of AE signals from the counts–duration relationship (duration ≡ end time − start time).
- AE energy: In this study, two energy measures were considered. The first is derived directly from the AE equipment, where the area below the signal curve is computed as an output parameter. This method of computing the AE signal energy will be referred to as "MACHINE". The second measure is the signal energy presented by RILEM [36]. In this second case, the AE signal energy is estimated as half of the rectangle area formed by the signal peak amplitude and its duration [36,77]. This alternative energy measure will be referred to as "RILEM".

2.3. Numerical Procedure Used in the Simulation: Discrete Element Method (LDEM)

A version of the discrete element method was used to perform the simulations. The main characteristic of this method is the possibility of naturally simulating the fracture and fragmentation in the system studied. In [78], several alternatives are revised using this method. Specifically, in the present case, a version of the discrete element method formed by elements proposed originally by [68] is used, here called the Lattice Discrete Element Method (LDEM). The LDEM approach represents solid systems as a set of uniaxial elements and nodal masses, forming regular cubic arrangements of cells of 20 bars and nine nodes each, as depicted in Figure 3a. The nodes have three degrees of freedom corresponding to the translations in the Euclidean Space. Two types of bars are used in the model, the normal bar L_n, that defines the cubic cell size, and the diagonal bars of length $L_d = \sqrt{3}L_n/2$. The properties of the LDEM elements with the elastic isotropic medium can be related using Equations (1) and (2),

$$\delta = \frac{9\nu}{4 - 8\nu},\ \alpha = \frac{9 + 8\delta}{2(9 + 12\delta)} \tag{1}$$

$$A_n = \alpha L_n^2,\ A_d = \frac{2}{\sqrt{3}}\delta\alpha L_n^2, \tag{2}$$

where ν denotes the material's Poisson ratio, whereas the normal and diagonal elements' initial axial stiffnesses are EA_n/L_n and EA_d/L_d, respectively, with E representing the material's Young's modulus. For ν = 0.25, the cubic array in Figure 3a yields the exact representation of the isotropic continuum, while other values of ν cause small differences to appear in the shear terms [79]. Other possibilities of arrangements and their link with other forms to define the stiffness of elements can be found in the literature [80].

To consider the possibility of representing nonlinear behavior, the softening law for quasi-brittle materials proposed by [81] is implemented using a triangular Element Constitutive Relationship (ECR) for the LDEM longitudinal and diagonal elements presented in Figure 3b, which allows accounting for the irreversible effects of crack nucleation and propagation.

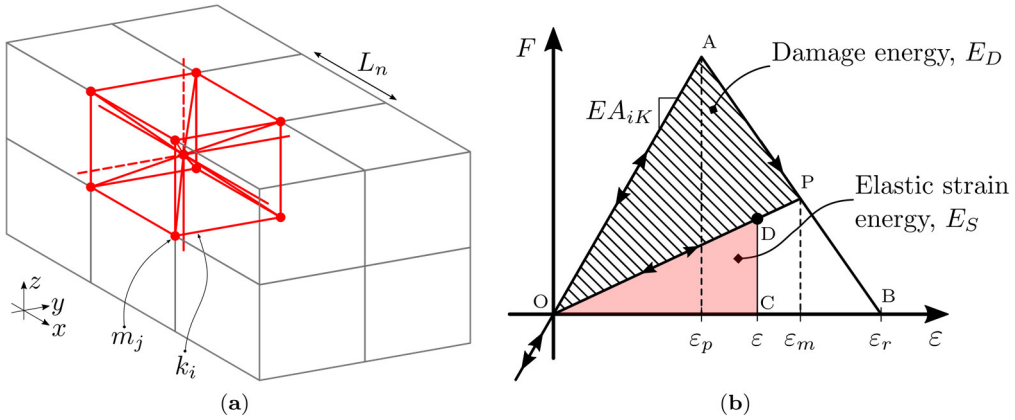

Figure 3. LDEM discretization strategy: (**a**) basic cubic module in the solid discretization and (**b**) constitutive law adopted for LDEM uniaxial elements. Adapted from [34,69,82] under the terms of the CC BY license.

Figure 3b describes the constitutive relation assumed by the LDEM model for the force exerted by a bar as a function of its strain, where ε_p represents a critical strain where a maximum force is reached for the bar.

The elastic limit strain, ε_m, is a local limit strain, and ε_r is the critical failure strain. Since the area under this curve is proportional to the energy accumulated by the bar as it undergoes deformation, for a given point P, the area of the triangle OAP (striped area) indicates the energy dissipated by damage, whereas the triangle OPC (gray area) is related to the elastic strain energy stored in the bar. If the external load is relaxed at the point P, the return slope is lower than the initial one because the element is partially damaged. When $\varepsilon = \varepsilon_r$, the damage energy density equals the fracture energy and the element fails, losing its load-carrying capacity. Each element's equivalent fracture area A_i^* is chosen to ensure that the energy dissipated by continuum fracture matches its discrete representation. For such purpose, the fracture of a cubic sample of dimensions $L_n \times L_n \times L_n$ is considered. Under compression, as the material is assumed to remain linearly elastic with the initial slope EA, failure is induced by indirect tension. In a quasi-brittle material, tensile collapse stress is commonly around 1/10, allowing the indirect capture of realistic behavior up to the body's maximum compression load. In addition to one of those approaches, the strains ε_p and ε_r are related to the material's equivalent length d_{eq} as follows by Equations (3) and (4),

$$\varepsilon_p = \sqrt{\frac{G_f}{E\, d_{eq}}}, \tag{3}$$

$$\varepsilon_r = \varepsilon_p d_{eq} \left(\frac{A_i^*}{A_i}\right)\left(\frac{2}{L_i}\right). \tag{4}$$

Here, G_F represents the fracture energy of the material. An important observation regards the physical meaning of d_{eq}, which represents the minimum length for a crack to propagate in unstable form. That is, if a crack with a length greater than d_{eq} develops in the structure, it will propagate in an unstable way when a critical level of loading is applied [79]. The equivalent length d_{eq} can be determined by means of the so-called Brittleness number proposed by Alberto Carpinteri [82,83], a dimensionless number defined according to Equation (5),

$$s = \frac{\left(\frac{G_f E}{D}\right)^{0.5}}{\sigma_p}, \tag{5}$$

where D represents the characteristic length of the structure and σ_p is the failure stress. As shown in [82], for the LDEM constitutive law, considering that $\sigma_p = E\ \varepsilon_p$, and combining Equations (3) and (5), it is possible to write

$$s = \frac{\left(\frac{G_f E}{D}\right)^{0.5}}{\sigma_p}. \quad (6)$$

In Equation (4), A_i^* is each element's equivalent fracture area, defined to ensure that the energy dissipated by fracture of the continuum equals that of its discrete counterpart. The sub-index indicates the type of element referenced (diagonal or normal). These relations are discussed in more detail in [82]. The random nature of the material was considered, perturbing the LDEM mesh and considering that the material's fracture energy G_F is a random field with a Weibull distribution characterized by a mean value variation coefficient and length correlation. After carrying out the spatial discretization, it is possible to write the Motion Equation presented by Equation (7),

$$\mathbf{M}\ddot{\mathbf{u}} + \mathbf{C}\,\dot{\mathbf{u}} + \mathbf{f} - \mathbf{p} = \mathbf{0}, \quad (7)$$

in which $\mathbf{u}$ is the vector of generalized nodal displacements, $\mathbf{M}$ is the diagonal mass matrix, $\mathbf{C}$ is the damping matrix, and $\mathbf{f}$ and $\mathbf{p}$ represent the internal and external forces acting on the nodal masses, respectively. If $\mathbf{M}$ and $\mathbf{C}$ are diagonal, the system is not coupled, and explicit central finite differences can be used to integrate the equations of motion in the time domain. As a result, since the nodal coordinates are updated at every time step, large displacements are accounted for naturally.

To ensure that the overall formulation is diagonal, the model's damping is assumed proportional to the mass (Equation (8)),

$$\mathbf{C} = D_f \mathbf{M} \quad (8)$$

where $D_f \cong 2\pi f_m \zeta_m$ is derived from the peak model's energy spectrum, with f_m and ζ_m representing the corresponding natural frequency and damping ratio, respectively.

The version of the discrete element method (LDEM) used in this study has been applied in previous publications from the research team [82,84]. Several references in which AE tests were simulated using the LDEM will also be discussed as follows.

The AE was simulated in the numerical model, capturing in the surface nodes the acceleration values during the damage process simulated. The area below the signals is a measure of the AE energy. The energy balance is also computed in each time step, that is, the Elastic, the Kinetic, and the Dissipated energies during the simulation (please refer to [39] for more details). In particular, the temporal derivative of the Kinetic energy computed is similar to the distribution of AE signals, but it does not consider the energy loss that could happen between the generation of the AE event and the detection of the signals by the AE sensors. In Figure 4a,b the energy balance when a typical event happens is described. It is understood that, when an event happens, an abrupt fall in the Elastic energy (E_{ele}) can be observed, with an abrupt increment in the Dissipated energy (E_d) due to the internal fracture in the system, and a fluctuation of Kinetic energy (E_k).

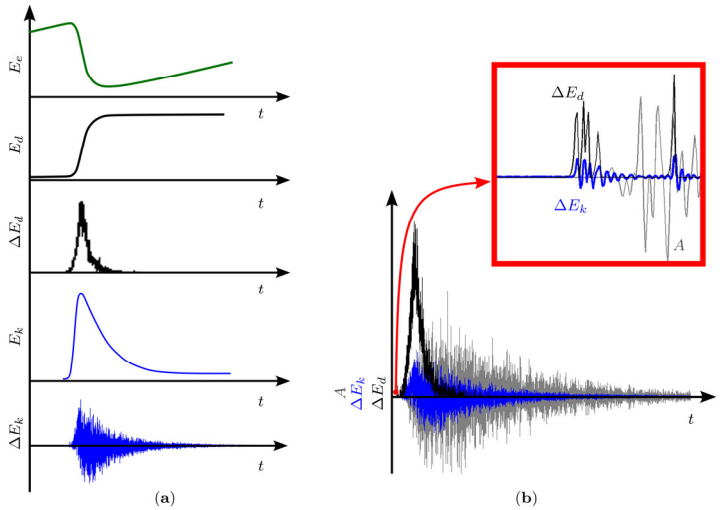

Figure 4. Qualitative link between the information computed during the energy balance and its relationship with the AE signal in the numerical model. (**a**) The time evolution of the Elastic energy (E_e), Dissipated energy (E_d), and Kinetic energy (E_k) in a typical time interval where an event happens. The time derivative of the Kinetic energy (ΔE_k) and Dissipated energy (ΔE_d) are also presented. (**b**) The superposition of the time derivative of the Kinetic energy (ΔE_k) and Dissipated energy (ΔE_d) with the AE signal captured in the AE device (A). The red box shows the initial region of (**b**) enlarged to perceive the delay between the arrival of the energy derivatives (ΔE_k, ΔE_d) and the AE signal (A). In the simulation, the energy changes are computed locally and instantly. However, to compute the energy of the AE signal, the mechanical wave induced by the event must travel through the specimen to reach the AE device. Only when it arrives at the device is it finally computed, which explains the observed delay. Adapted with permission from [39], copyright 2013, Elsevier.

Figure 4a presents the superposition of the AE signal captured in a virtual sensor on the numerical model surface (A), and the changes in Kinetic energy $\Delta E_k(t)$ and Dissipated energy $\Delta E_d(t)$. The similarity between the AE signal signature A(t) and $\Delta E_k(t)$ is evident. Finally, in Figure 4b, the delay between A(t) and $\Delta E_k(t)$ is shown. $\Delta E_k(t)$ is directly computed from the Kinetic energy calculated in the energy balance during the simulation. However, $\Delta E_k(t)$ is computed when the event occurs, whereas the AE signal A(t) experiences a delay compared to $\Delta E_k(t)$. The delay occurs since the AE signal is captured by the AE device after the arrival of the elastic wave. These aspects are discussed in [39].

Regarding the self-healing process studied in this work, the LDEM provides three valuable characteristics for the analysis: first, it allows us to obtain the energy balance (Elastic, Kinetic, and Dissipated energies); second, it can successfully reproduce AE tests; and third, it can also model the test used to compute the fracture energy, in accordance with experimental works. In fact, in a previous work published by some of the authors, the LDEM was used for the simulation of AE tests in quasi-brittle materials (similar to the ones considered in the current work) [69]. Other approaches using discrete element methods have been used by other authors to simulate the self-healing process in concrete, but without including AE tests ([66,67]).

2.4. Numerical Model Using LDEM for a Beam with and Without Self-Healing Capability

To obtain insights into the change in the fracture energy due to the triggering of the self-healing mechanism, numerical simulations were performed to reproduce the behavior of the VI specimens during the pre-cracking tests, and of the corresponding SH specimens during the re-loading tests. The following procedure was used. Initially, the capsule containing the healing agent was modeled with elements with no stiffness, because the resin inside it is liquid in the initial state, and hence it cannot provide any contribution in

terms of stiffness. The capsule is indicated as the green region in Figure 5. The pre-crack was modeled by weakening elements in the central region. After simulating the virgin specimen and reaching the maximum load, significant damage occurred, and the specimen was unloaded. In this configuration, the area within the capsule and its surroundings contained a substantial number of completely broken elements, exceeding the deformation level $\varepsilon_{max} > \varepsilon_r$. At this point, it was determined that the simulation of the pre-cracking of the virgin specimen was complete.

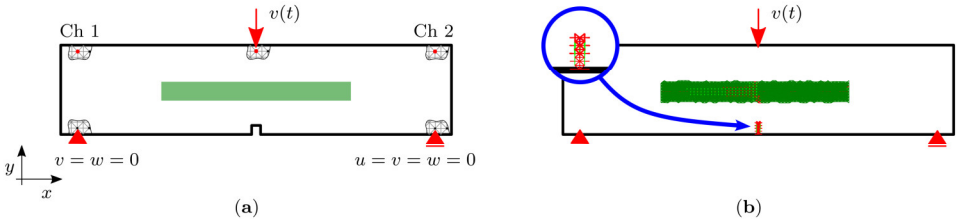

Figure 5. LDEM numerical model (**a**), schematic view, representing the boundary conditions and model acting forces, and (**b**) the discretization level in the notch region and in the cylinder with the resin.

The self-healing transformation was then activated. This was achieved by considering that the broken elements possessed new strength properties after the expansion and subsequent polymerization of the resin inside the crack, and their initial length was equal to the length reached at the conclusion of the virgin specimen simulation. The elements with partial damage, characterized by a deformation level ε_{max} ranging between ε_r and ε_p ($\varepsilon_r > \varepsilon_{max} > \varepsilon_p$), remained unmodified. This hypothesis assumes that, if the elements were not completely broken, the resin did not reach their position, and the self-healing effect was not present. In the second part, the capsule region and its surroundings assumed the new strength properties. In the current implementation, the pre-crack region corresponding to the notch was not healed in the simulation because of the relatively big gap between the notch faces (4 mm). However, as shown in Figure 1c,d, the PU resin was able to expand not only in the crack region but also in the notch, solidly adhering to its faces. Therefore, to provide a more realistic simulation, this criterion will be further studied in the ongoing research, along with other parameters that govern the simulation of the healing process.

In Table 1, the material properties considered for the cement mortar and for the hardened polyurethane resin (PU) are presented. Three possible values of fracture energy for PU were considered. The mechanical properties of the cement mortar (E = 2.18 GPa, $G_f^{LDEM,VI}$ = 80 N/m, $\sigma_p = E\,\varepsilon_p$= 4 MPa) were calibrated by means of the pre-cracking results. Using Equation (3), these material parameters could be translated as the input properties presented in Table 1. Notice that the value of d_{eq} in the present case is d_{eq} = 0.01 m. As discussed in [83], d_{eq} may be regarded as a material property, since it does not depend on the discretization level of the numerical model mesh. Moreover, when a crack of this length nucleates inside the specimen, it could propagate in unstable form under a critical level of stress.

For the PU for the SH specimens, the input density was maintained, and the Young's modulus was adopted as E = 2 GPa. The three possible values for the fracture energy of the PU are a "weak" one ($G_f^{LDEM,PU,inp}$ = 35 N/m, σ_p= E ε_p = 0.36 MPa), an "intermediate" one ($G_f^{LDEM,PU,inp}$ = 70 N/m, σ_p = 0.51 MPa), and a "strong" one ($G_f^{LDEM,PU,inp}$ = 140 N/m, σ_p = 0.73 MPa). By utilizing Equation (3) once again, it was feasible to compute a consistent value of d_{eq} = 0.5 m for the three SH specimens' input data. In other words, the self-healing mechanism introduced in the damaged regions a material (PU) with reduced strength, but with enhanced ductility. It should be noted that the aim of these simulations

was not to replicate experimental findings, but rather to aid in the understanding of the healing mechanism.

Table 1. The input parameters used in the numerical model.

Material Property	Value		
Density (ρ)	2000 kg/m^3		
Mortar fracture energy ($G_f^{LDEM,VI,inp}$)	80 N/m		
Poisson Ratio (ν)	0.25		
Equivalent length $d_{eq}{}^{v}$ (m)	0.01		
PU fracture energy ($G_f^{LDEM,PU,inp}$) *	35 N/m	70 N/m	140 N/m
Equivalent length $d_{eq}{}^{SH}$ (m)	0.50		
Coefficient of fracture energy variation (CV_{Gf})	100%		
LDEM cubic cell side	1.0×10^{-3} m		
Number of cubic cells (width by height by length)	$103 \times 41 \times 41$		

* Three different values of fracture energy were tested, as will be discussed.

3. Results

3.1. Measurement of the Specific Fracture Energy: Comparison Between Experimental and Numerical Results

The results on the specific fracture energy obtained experimentally (mechanical and AE tests) and numerically (LDEM simulations) are reported graphically in Figures 6–11 and discussed in the following.

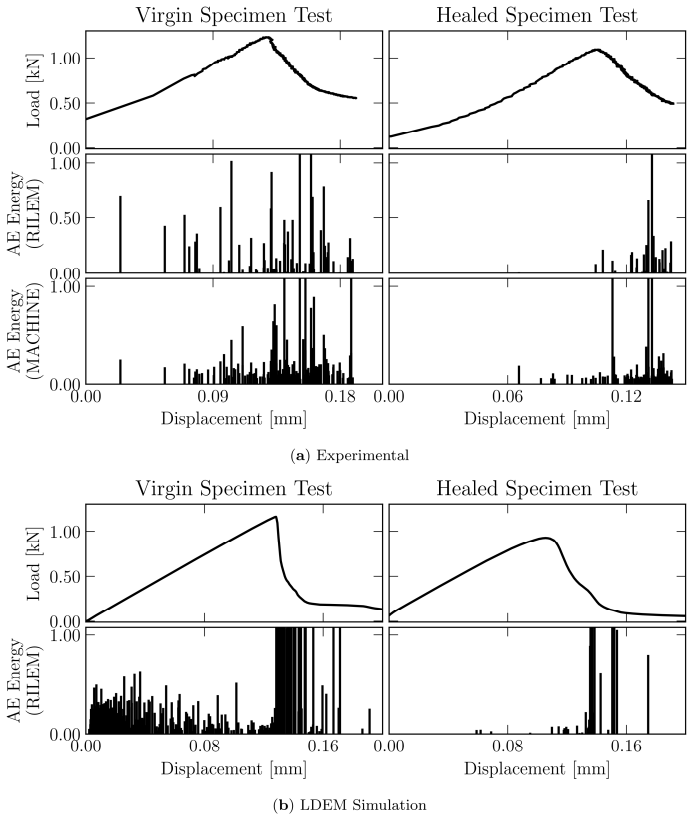

(**a**) Experimental

(**b**) LDEM Simulation

Figure 6. The load vs. displacement and AE energy signal (**a**) for one experimental test and (**b**) for the LDEM simulation, considering the input data presented in Table 1 for the "intermediate" resin with $G_f^{LDEM,PU,inp}$ = 70 N/m. (**Left**): virgin specimen test (pre-cracking); (**right**): SH specimen test (re-loading). The AE energy plots were normalized with arbitrary values for the sake of visualization, 0.05 for the RILEM and 6 for the MACHINE.

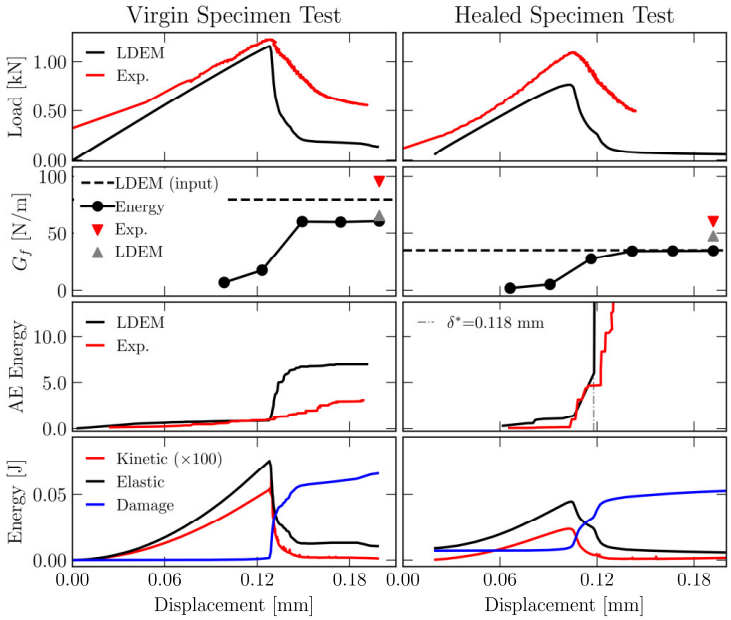

Figure 7. Experimental and numerical results considering the "weak" resin, $G_f^{LDEM,PU,inp}$ = 35 N/m. (**Left**): virgin specimen (pre-cracking) test; (**right**): SH specimen (re-loading) test. Note: the Kinetic, Elastic, and Damage energies are from the numerical model. The AE energy was normalized with respect to the AE energy at the peak load.

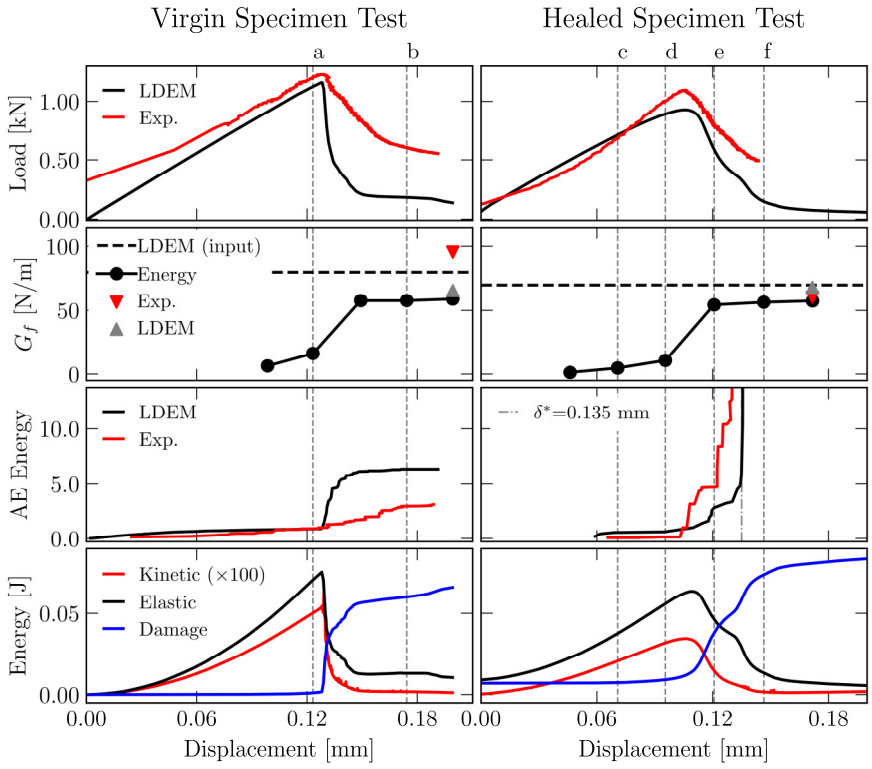

Figure 8. Experimental and numerical results considering the "intermediate" resin, $G_f^{LDEM,PU,inp}$ = 70 N/m. (**Left**): virgin specimen test (pre-cracking); (**right**): SH specimen (re-loading) test. The vertical lines (a)–(f) are linked with the measurement of the ligament area sL(δ) shown in Figure 10. Note: the Kinetic, Elastic, and Damage energies are from the numerical model. The AE energy was normalized with respect to the AE energy at the peak load.

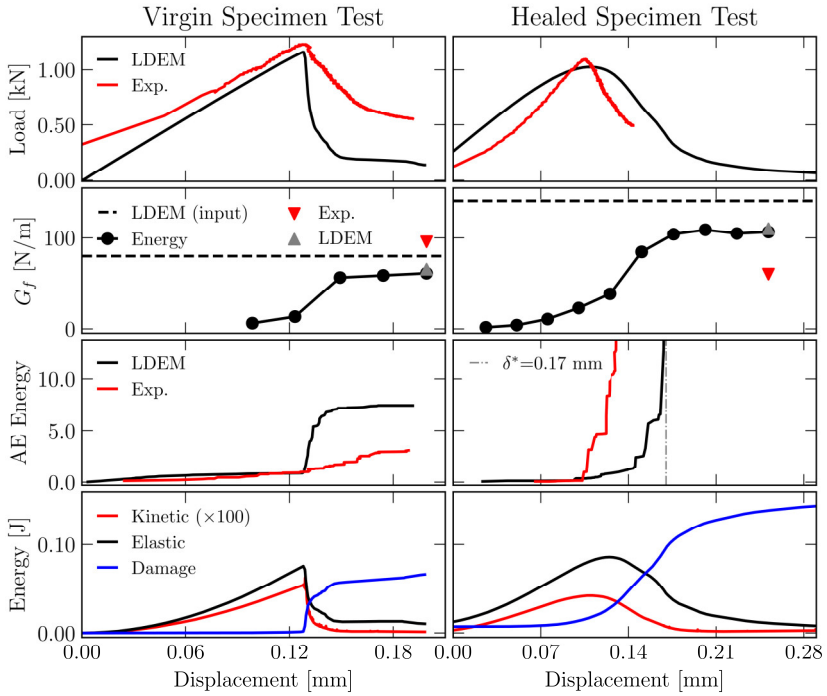

Figure 9. Experimental and numerical results considering the "strong" resin, $G_f^{LDEM,PU,inp}$ = 140 N/m. (**Left**): virgin specimen (pre-cracking) test; (**right**): SH specimen (re-loading) test. Note: the Kinetic, Elastic, and Damage energies are from the numerical model. The AE energy was normalized with respect to the AE energy at the peak load.

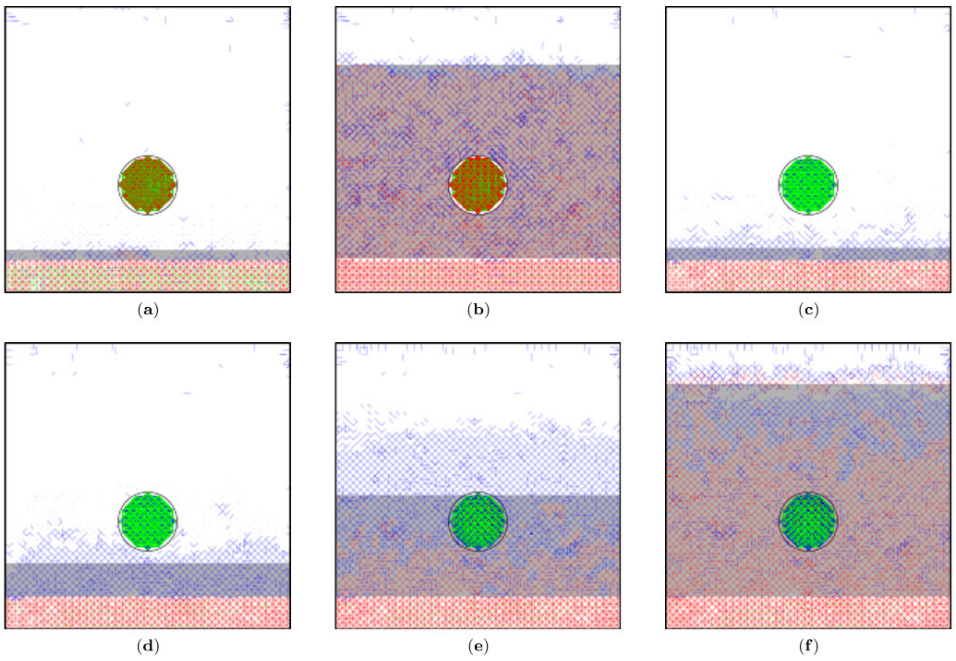

Figure 10. The fracture surface of the $G_f^{LDEM,PU,inp}$ = 70 N/m model with the partial configuration. (**a**–**f**) correspond to the dashed lines (a)–(f) in Figure 8. Broken bars are indicated in red, damaged bars in blue, and resin bars in green.

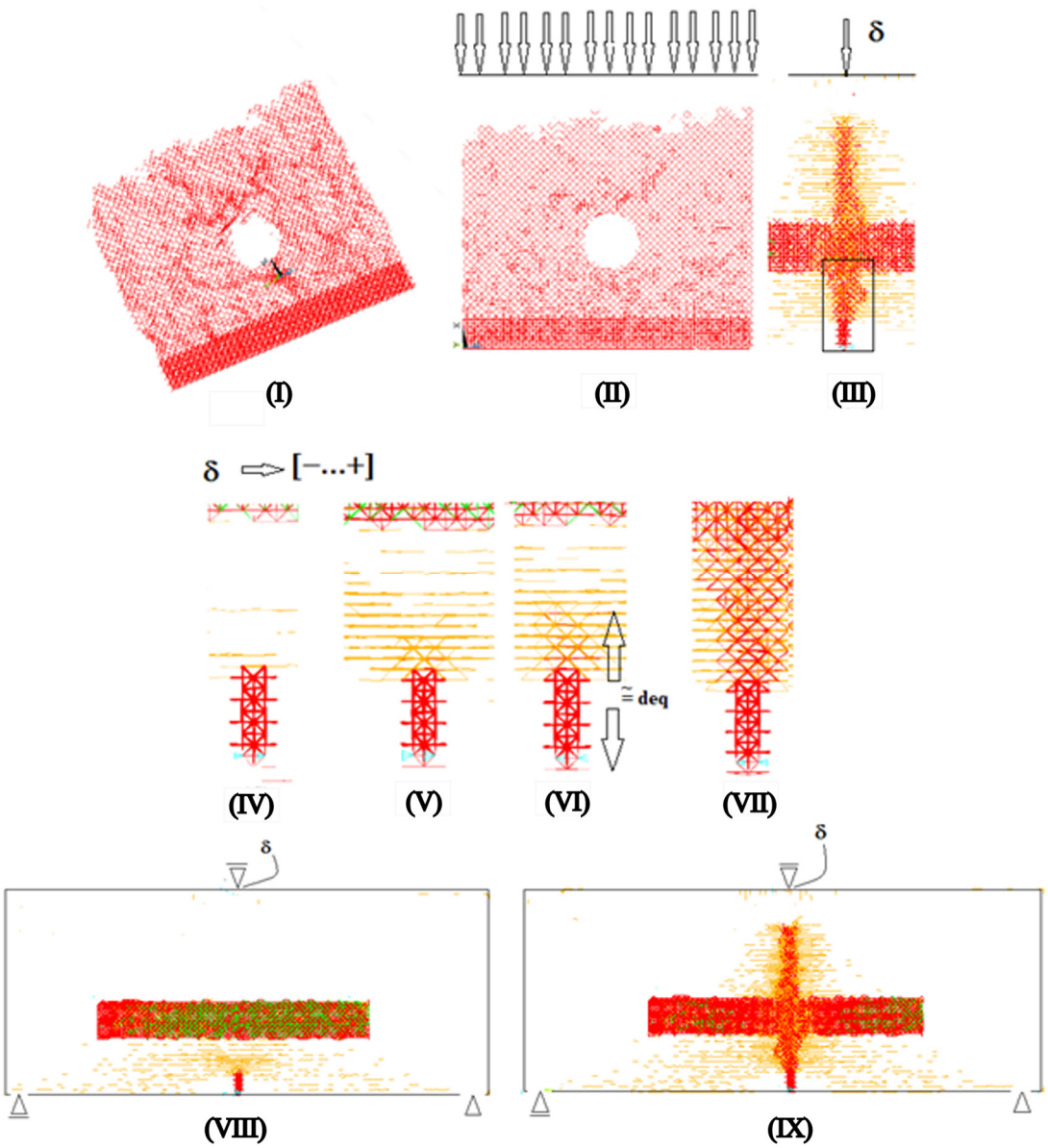

Figure 11. Different views of the partial configuration obtained with the LDEM model. Broken bars are indicated in red, damaged bars in orange and resin bars in green. Cyan points correspond to control points for crack opening measurements. (**I–III**): The broken element distribution after the virgin specimen reaches the maximum load: (**I**) oblique, (**II**) transversal, and (**III**) lateral views. (**IV–VII**): The lateral view of the broken and damaged bars, as delimited in the black box in (**III**), for increasing levels of the vertical prescribed displacement, δ. (**VIII**,**IX**): Lateral views of the specimen, where only the damaged (orange) and broken (red) bars are visualized.

To determine the experimental fracture energy G_f of the specimen, the W_0 energy was first calculated as the area under the load-displacement curve [85] which was obtained via the trapezoidal rule (Equation (9)),

$$W_0 = \sum_{i=2}^{N} (\delta_i - \delta_{i-1})\left(\frac{F_i + F_{i-1}}{2}\right) \quad (9)$$

where δ and F are, respectively, the displacement of the piston (in mm) and the force (in Newtons) measured by the testing machine at two consecutive data points i and $i - 1$, and

N is the total number of data points acquired during the test. Then, to obtain the fracture energy, the W_0 energy was divided by the virgin specimen ligament area (Equation (10)),

$$G_{f,0}^{exp} = \frac{W_0}{s_L} \quad (10)$$

In the experimental case, the ligament area used was considered as (40 mm × 36 mm), that is, the cross-section area minus the notch area (40 mm × 4 mm). This procedure was adopted because measurements of the ligament area during the experimental test were not performed. This measure of $G_{f,0}$ was computed in two ways using both the experimental data and using the LDEM information. The two measures will be referred to as $G_{f,0}{}^{exp}$ and $G_{f,0}{}^{LDEM}$, respectively.

The dissipated energy can be calculated in various configurations during the numerical simulation. As a matter of fact, in each configuration, the dissipated energy for a specific prescribed vertical displacement (δ), known as $W_{dis}(\delta)$, can be determined. Correspondingly, the ligament area can be identified in this configuration.

The ligament areas reported in Figure 10a–f correspond to the dashed lines (a)–(f) in Figure 8. This ligament area $s_L(\delta)$ was computed as a weighted mean considering the broken and damaged elements in the specimen cross-section. The broken elements had a weight of 1.0 and the damaged ones had weight varying between [0.0, 1.0], relative to their level of damage. With these considerations, the alternative measure of fracture energy $G_f{}^{LDEM}(\delta)$ can be defined by Equation (11),

$$G_f^{LDEM}(\delta) = \frac{W_{dis}(\delta)}{S_L(\delta)} \quad (11)$$

Figure 6 presents the evolution of the AE results vs. the prescribed displacement applied for one experiment, and its corresponding LDEM simulation. Specifically, the AE energy is shown using both the RILEM and MACHINE measurements previously defined for the experimental results. The numerical model is defined with the input data presented in Table 1, considering an "intermediate" resin with $G_f{}^{LDEM,PU,inp}$ = 70 N/m.

Figures 7–9 show the results for the healed cases, "weak", "intermediate", and "strong", following Table 1. The experimental and numerical measures of the fracture energy are consistent. In fact, the possibility of computing the fracture energy evolution measuring $G_f{}^{LDEM}(\delta)$ could be complementary information to understand how the fracture energy $G_{f,0}{}^{exp}$ is reached. Notice that the results regarding the virgin specimens presented in Figures 7–9 are slightly different because, in each simulation, a different set of random parameters (with the same statistical distribution) was considered.

The load vs. prescribed displacement plots (first row) are presented for the virgin (pre-cracking) and for the SH (re-loading) test, with the experimental results presented in red and the LDEM results presented in black. The intermediate value of the PU fracture energy (Figure 8) was the one that better approximated the experimental results. The initial elastic slope and the peak load value were captured well, although a better adjustment is necessary to capture the post-peak behavior. In particular, in the numerical simulations, the residual strength was lower. This is considered to be acceptable for the purposes of this study, because the residual strength depends on complex mechanics related to material behavior, and simulating it is beyond the scope of our analysis in this work. Capturing the post-peak behavior in both the virgin and self-healing specimens could be a focus for the continuation of the research presented in this study.

In the second row of Figures 7–9, different values of G_f are presented. In the slashed horizontal line, the input values used for the LDEM model are represented called, in the plots, LDEM (input). These values also appear in Table 1, and the ^{GfLDEM,VI,inp} = 80 N/m

for the virgin specimens and $G_f^{LDEM,PU,inp}$ = 35, 70, 140 N/m for the SH specimens. The $G_{f,0}^{exp}$ (red triangle) and $G_{f,0}^{LDEM}$ (gray triangle) are computed using Equation (10). Also, the evolution of the fracture energy during the LDEM simulation, $G_f^{LDEM}(\delta)$, computed with Equation (11), is indicated in the plots with black lines and circular dots.

In the third row of Figures 7–9, the Accumulated AE energy is presented. In these plots, only the signals produced by Sensor 1, indicated with "Ch1" in Figure 5a, were considered. The Accumulated AE Energy was measured using the RILEM procedure. In the comparison between numerical and experimental results, the difference between the two curves of the Accumulated AE Energy is evident after the post-peak is reached.

Finally, in the fourth and last row of Figures 7–9, the numerical energy balance is presented.

In Figures 7–9, the SH specimen tests simulated using the LDEM are presented. A characteristic displacement (δ*) can be defined in the simulation of the SH specimens as the moment when the Accumulated AE energy begins to increase abruptly (the AE energy values were normalized with respect to the AE energy in the peak load). In this case, the characteristic displacement indicates the transition moment from AE "silence" to increased AE activity. A smaller value of δ* would possibly indicate that the specimen in question emits more AE energy than a specimen with a larger value of δ*. The premise being adopted is that a specimen that starts to emit AE energy before (in the sense of the duration of the experiment) will emit more AE energy overall than a specimen that starts to emit AE energy later. In this sense, the characteristic displacement δ* could have a direct correlation with the fracture energy Gf. A specimen with small Gf cannot absorb much deformation energy and would tend to emit AE energy after small amounts of deformation (small δ*). This hypothesis would have to be verified in further works by investigating more experimental and numerical results.

Furthermore, analyzing (for the SH specimen simulation) the relationship between fracture energy (the $G_{f,0}^{LDEM}$ indicated with a gray triangle in Figures 7–9) and characteristic displacement (δ*), the following behavior is observed: δ* = 0.17 mm for $G_{f,0}^{LDEM}$ = 105 N/m, δ* = 0.135 mm for $G_{f,0}^{LDEM}$ = 68 N/m, and δ* = 0.118 mm for $G_{f,0}^{LDEM}$ = 45 N/m. That indicates an inverse correlation between the intensity of AE activity and the fracture energy of the SH specimen, which agrees with the experimental results presented in Section 3.2.

In Figure 10, the specimen cross-sections for the partial configurations (a)–(f) presented in Figure 8 to compute the ligament area $s_L(\delta)$ are used in Equation (9) to define the fracture energy $G_f^{LDEM}(\delta)$.

Finally, in Figure 11, the view of different configurations obtained with the LDEM are presented. In Figure 11VI, it can be seen that, immediately before the main crack propagated in unstable form in the virgin specimen simulation, its length was approximately $10 \times L_n$ = 0.001 m, then close to d_{eq} = 0.01 m. The pre-crack (corresponding to the notch) grew in subcritical form up to arrive to a length close to d_{eq}, and then propagated in unstable form. This is coherent with the definition of d_{eq} presented in the description of the LDEM formulation.

3.2. Combined Analysis of Fracture Energy and AE Energy

Finally, the tendency of the specimen toughness to increase (or decrease) in relation to AE parameters was investigated. The purpose of this analysis was to determine if there could be a correlation between critical fracture energy measured ($G_{f,0}^{exp}$) and some typical characteristics of AE signals that will be discussed as follows. In Figure 12, six values for fracture energy computed using Equation (10) over the experimental tests data are presented (three of virgin specimens and three of SH specimens).

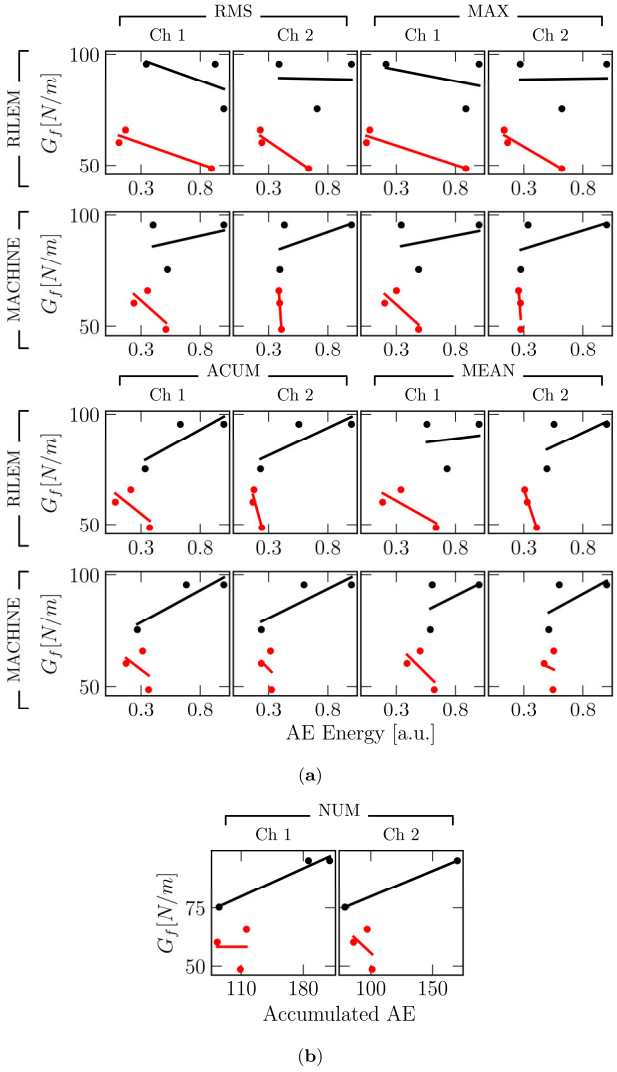

(**a**)

(**b**)

Figure 12. The overall experimental results of post-processing fracture energy vs. the intensity of AE activity. Dots indicate experimental values, continuous lines the tendency. The data for the virgin specimens are shown in black, and for the SH specimens in red. (**a**) Results in terms of fracture energy Gf measured vs. different measurements of AE energy in arbitrary units [a.u]. AE units are normalized for each measure ("RMS", "MAX", "ACUM", "MEAN") with respect to its maximum value among all specimens. The measure of AE energy is presented in terms of the Root Mean Square of the AE signal energy (RMS), the Maximum of the AE signal energy (MAX), the Accumulated signal energy (ACUM), and the Mean value of the AE signal energy (MEAN). RILEM and MACHINE are references to the procedure used to measure the AE energy. (**b**) Gf vs. accumulated Number of AE signals (NUM). Ch1 and Ch2 indicate the sensors used in the tests, placed as illustrated in Figure 1a.

The results obtained are presented for both the RILEM and MACHINE measurements of AE energy, utilizing the signal energy measurements from the AE sensors.

The characteristics of AE signals considered are:

1. The RMS value of the AE energy (RMS);
2. The maximum value of signal energy (MAX);
3. The accumulated value of AE energy (ACUM);
4. The mean value of the AE energy (MEAN);
5. The total number of AE signals recorded (NUM).

For the virgin samples, as depicted in Figure 12 with a black line, there was no definitive pattern in the correlation between fracture energy and the measured AE signal activity. However, excluding the diagrams in the first row, it can be stated that, generally, an

increase in AE activity was noticeable when the fracture energy of the specimens increased. However, for the SH specimens, a reverse pattern was observed where an increase in AE activity corresponded to a decrease in specimen fracture energy, as shown by the red line in Figure 12. To reinforce this trend, it is essential to collect more experimental results during the ongoing research.

4. Conclusions

The present study investigates the mechanical behavior of cement mortar specimens subjected to three-point bending tests, with a self-healing mechanism activated after damage. The experimental work was conducted in a previous study by the research team. After pre-cracking of the virgin specimens and the curing of the polyurethane resin (PU) responsible for the self-healing effect, a second test was conducted to assess the effectiveness of the healing process. Continuing monitoring of the specimens' behavior during the mechanical tests was conducted via Acoustic Emission (AE) tests. The investigations presented here extend the analysis of the experimental results through the combined application of the Lattice Discrete Element Method (LDEM), a numerical method for modeling fracture in solids and simulating AE tests.

The main conclusion of this study is that, in general, the self-healed specimens showed a negative correlation between (absorbed) fracture energy and (emitted) AE energy. In other words, the more energy a specimen can absorb, the less energy it emits. This is plausible, because the total energy a specimen can release is the sum of the absorbed and emitted parts. When the PU resin is introduced, it introduces a softening behavior that favors energy absorption instead of emission by means of AE activity, which can be regarded as a measure of tenacity.

This study also presents the LDEM as a viable numerical tool that can be of aid for simulating self-healed materials. The LDEM simulations presented the same fracture energy vs. AE energy trends found in the experimental results. The LDEM allowed for the computation of changes in the ligament and fracture energy during simulation, complementing the information obtained from experimental tests.

Future studies could focus on using the LDEM for investigating the stress distribution in the specimen, as it is likely modified with the introduction of the PU resin. We also believe that further tests need to be conducted in the continuation of the present research to consolidate the trend presented in Figure 12. Additionally, experimental tests on similar specimens (without the self-healing effect) should be carried out to verify how the healing effect influences the mechanical behavior of the specimens.

Author Contributions: Conceptualization, P.M.M., B.N.R.T., I.I., P.A., G.A. and G.L.; methodology, P.M.M., B.N.R.T., I.I., P.A, G.A. and G.L.; software, B.N.R.T., I.I. and P.M.M.; validation, B.N.R.T., I.I., P.M.M. and G.L.; formal analysis, B.N.R.T., I.I., P.M.M. and G.L.; investigation, B.N.R.T., I.I., P.M.M. and G.L.; resources, P.A., G.A., J.-M.T., I.I. and G.L.; data curation, P.M.M., B.N.R.T., and I.I.; writing—original draft preparation, P.M.M., B.N.R.T., P.A., G.A., J.-M.T. and I.I.; writing—review and editing, P.M.M., B.N.R.T., I.I., P.A., G.A. and G.L.; visualization, B.N.R.T., I.I. and P.M.M.; supervision, P.A., G.L. and I.I.; project administration, P.M.M., G.L., I.I. and P.A.; funding acquisition, P.A., G.L. and I.I. All authors have read and agreed to the published version of the manuscript.

Funding: This research received no external funding.

Institutional Review Board Statement: Not applicable.

Informed Consent Statement: Not applicable.

Data Availability Statement: The raw data supporting the conclusions of this article will be made available by the authors on request.

Acknowledgments: The authors acknowledge the financial support received from the Brazilian National Council for Scientific and Technological Development (CNPq, Brazil) and from the Coordination for the Improvement of Higher Education Personnel (CAPES-Brazil). The financial aid of the sponsorship provided by Politecnico di Torino, Italy, with basic research funds is also acknowledged.

Conflicts of Interest: The authors declare no conflicts of interest.

References

1. Van Tittelboom, K.; De Belie, N. Self-Healing in Cementitious Materials—A Review. *Materials* **2013**, *6*, 2182–2217. [CrossRef] [PubMed]
2. Olivier, K.; Darquennes, A.; Benboudjema, F.; Gagné, R. Early-Age Self-Healing of Cementitious Materials Containing Ground Granulated Blast-Furnace Slag under Water Curing. *ACT* **2016**, *14*, 717–727. [CrossRef]
3. Qureshi, T.; Kanellopoulos, A.; Al-Tabbaa, A. Autogenous self-healing of cement with expansive minerals-II: Impact of age and the role of optimised expansive minerals in healing performance. *Constr. Build. Mater.* **2019**, *194*, 266–275. [CrossRef]
4. Cuenca, E.; Mezzena, A.; Ferrara, L. Synergy between crystalline admixtures and nano-constituents in enhancing autogenous healing capacity of cementitious composites under cracking and healing cycles in aggressive waters. *Constr. Build. Mater.* **2021**, *266*, 121447. [CrossRef]
5. Doostkami, H.; Formagini, S.; Serna, P.; Roig-Flores, M. Effects of healing start time and duration on conventional and high-performance concretes incorporating SAP, crystalline admixture, and sepiolite: A comparative study. *Case Stud. Constr. Mater.* **2024**, *20*, e02835. [CrossRef]
6. Snoeck, D.; Steuperaert, S.; Van Tittelboom, K.; Dubruel, P.; De Belie, N. Visualization of water penetration in cementitious materials with superabsorbent polymers by means of neutron radiography. *Cem. Concr. Res.* **2012**, *42*, 1113–1121. [CrossRef]
7. Lefever, G.; Charkieh, A.S.; Abbass, M.; Van Hemelrijck, D.; Snoeck, D.; Aggelis, D.G. Ultrasonic evaluation of self-healing cementitious materials with superabsorbent polymers: Mortar vs. concrete. *Dev. Built Environ.* **2023**, *13*, 100112. [CrossRef]
8. Van Tittelboom, K.; Wang, J.; Araújo, M.; Snoeck, D.; Gruyaert, E.; Debbaut, B.; Derluyn, H.; Cnudde, V.; Tsangouri, E.; Van Hemelrijck, D.; et al. Comparison of different approaches for self-healing concrete in a large-scale lab test. *Constr. Build. Mater.* **2016**, *107*, 125–137. [CrossRef]
9. Alghamri, R.; Kanellopoulos, A.; Al-Tabbaa, A. Impregnation and encapsulation of lightweight aggregates for self-healing concrete. *Constr. Build. Mater.* **2016**, *124*, 910–921. [CrossRef]
10. Riordan, C.; Anglani, G.; Inserra, B.; Palmer, D.; Al-Tabbaa, A.; Tulliani, J.-M.; Antonaci, P. Novel production of macrocapsules for self-sealing mortar specimens using stereolithographic 3D printers. *Cem. Concr. Compos.* **2023**, *142*, 105216. [CrossRef]
11. Al-Tabbaa, A.; Litina, C.; Giannaros, P.; Kanellopoulos, A.; Souza, L. First UK field application and performance of microcapsule-based self-healing concrete. *Constr. Build. Mater.* **2019**, *208*, 669–685. [CrossRef]
12. Shields, Y.; De Belie, N.; Jefferson, A.; Van Tittelboom, K. A review of vascular networks for self-healing applications. *Smart Mater. Struct.* **2021**, *30*, 063001. [CrossRef]
13. Zhang, W.; Zheng, Q.; Ashour, A.; Han, B. Self-healing cement concrete composites for resilient infrastructures: A review. *Compos. Part B Eng.* **2020**, *189*, 107892. [CrossRef]
14. Van Den Heede, P.; Mignon, A.; Habert, G.; De Belie, N. Cradle-to-gate life cycle assessment of self-healing engineered cementitious composite with in-house developed (semi-)synthetic superabsorbent polymers. *Cem. Concr. Compos.* **2018**, *94*, 166–180. [CrossRef]
15. Garces, J.I.T.; Dollente, I.J.; Beltran, A.B.; Tan, R.R.; Promentilla, M.A.B. Life cycle assessment of self-healing geopolymer concrete. *Clean. Eng. Technol.* **2021**, *4*, 100147. [CrossRef]
16. Maddalena, R.; Sweeney, J.; Winkles, J.; Tuinea-Bobe, C.; Balzano, B.; Thompson, G.; Arena, N.; Jefferson, T. Applications and Life Cycle Assessment of Shape Memory Polyethylene Terephthalate in Concrete for Crack Closure. *Polymers* **2022**, *14*, 933. [CrossRef]
17. Panza Uguzzoni, A.M.; Fregonara, E.; Ferrando, D.G.; Anglani, G.; Antonaci, P.; Tulliani, J.-M. Concrete Self-Healing for Sustainable Buildings: A Focus on the Economic Evaluation from a Life-Cycle Perspective. *Sustainability* **2023**, *15*, 13637. [CrossRef]
18. Bandeira Barros, L.; Knockaert, M.; Tenório Filho, J.R. Towards a more sustainable construction industry: Bridging the gap between technical progress and commercialization of self-healing concrete. *Constr. Build. Mater.* **2023**, *403*, 133094. [CrossRef]
19. Di Summa, D.; Ferrara, L.; De Belie, N. How to account for benefits of Self-Healing concrete in design? A LCA/LCC perspective. In Proceedings of the 14th FIB PhD Symposium in Civil Engineering, Rome, Italy, 5–7 September 2022; pp. 689–696, ISBN 978-294064317-2.
20. Di Summa, D.; Parpanesi, M.; Ferrara, L.; De Belie, N. A holistic life cycle design approach to enhance the sustainability of concrete structures. *Struct. Concr.* **2023**, *24*, 7684–7704. [CrossRef]

21. Van Mullem, T.; Anglani, G.; Dudek, M.; Vanoutrive, H.; Bumanis, G.; Litina, C.; Kwiecień, A.; Al-Tabbaa, A.; Bajare, D.; Stryszewska, T.; et al. Addressing the need for standardization of test methods for self-healing concrete: An inter-laboratory study on concrete with macrocapsules. *Sci. Technol. Adv. Mater.* **2020**, *21*, 661–682. [CrossRef]
22. Cappellesso, V.; Di Summa, D.; Pourhaji, P.; Prabhu Kannikachalam, N.; Dabral, K.; Ferrara, L.; Cruz Alonso, M.; Camacho, E.; Gruyaert, E.; De Belie, N. A review of the efficiency of self-healing concrete technologies for durable and sustainable concrete under realistic conditions. *Int. Mater. Rev.* **2023**, *68*, 556–603. [CrossRef]
23. Lo Monte, F.; Repesa, L.; Snoeck, D.; Doostkami, H.; Roig-Flores, M.; Jackson, S.J.P.; Alvarez, A.B.; Nasner, M.; Borg, R.P.; Schröfl, C.; et al. Multi-performance experimental assessment of autogenous and crystalline admixture-stimulated self-healing in UHPFRCCs: Validation and reliability analysis through an inter-laboratory study. *Cem. Concr. Compos.* **2024**, *145*, 105315. [CrossRef]
24. Feiteira, J.; Tsangouri, E.; Gruyaert, E.; Lors, C.; Louis, G.; De Belie, N. Monitoring crack movement in polymer-based self-healing concrete through digital image correlation, acoustic emission analysis and SEM in-situ loading. *Mater. Des.* **2017**, *115*, 238–246. [CrossRef]
25. Hilloulin, B.; Legland, J.-B.; Lys, E.; Abraham, O.; Loukili, A.; Grondin, F.; Durand, O.; Tournat, V. Monitoring of autogenous crack healing in cementitious materials by the nonlinear modulation of ultrasonic coda waves, 3D microscopy and X-ray microtomography. *Constr. Build. Mater.* **2016**, *123*, 143–152. [CrossRef]
26. Lefever, G.; Snoeck, D.; De Belie, N.; Van Vlierberghe, S.; Van Hemelrijck, D.; Aggelis, D.G. The Contribution of Elastic Wave NDT to the Characterization of Modern Cementitious Media. *Sensors* **2020**, *20*, 2959. [CrossRef]
27. Snoeck, D.; Malm, F.; Cnudde, V.; Grosse, C.U.; Van Tittelboom, K. Validation of Self-Healing Properties of Construction Materials through Nondestructive and Minimal Invasive Testing. *Adv. Mater. Interfaces* **2018**, *5*, 1800179. [CrossRef]
28. Gliozzi, A.S.; Scalerandi, M.; Anglani, G.; Antonaci, P.; Salini, L. Correlation of elastic and mechanical properties of consolidated granular media during microstructure evolution induced by damage and repair. *Phys. Rev. Mater.* **2018**, *2*, 013601. [CrossRef]
29. Tsangouri, E.; Aggelis, D.G.; Van Tittelboom, K.; De Belie, N.; Van Hemelrijck, D. Detecting the Activation of a Self-Healing Mechanism in Concrete by Acoustic Emission and Digital Image Correlation. *Sci. World J.* **2013**, *2013*, 424560. [CrossRef]
30. Tsangouri, E.; Gilabert, F.A.; De Belie, N.; Van Hemelrijck, D.; Zhu, X.; Aggelis, D.G. Concrete fracture toughness increase by embedding self-healing capsules using an integrated experimental approach. *Constr. Build. Mater.* **2019**, *218*, 424–433. [CrossRef]
31. Tsangouri, E.; Karaiskos, G.; Deraemaeker, A.; Van Hemelrijck, D.; Aggelis, D. Assessment of Acoustic Emission localization accuracy on damaged and healed concrete. *Constr. Build. Mater.* **2016**, *129*, 163–171. [CrossRef]
32. Tsangouri, E.; Lelon, J.; Minnebo, P.; Asaue, H.; Shiotani, T.; Van Tittelboom, K.; De Belie, N.; Aggelis, D.G.; Van Hemelrijck, D. Feasibility study on real-scale, self-healing concrete slab by developing a smart capsules network and assessed by a plethora of advanced monitoring techniques. *Constr. Build. Mater.* **2019**, *228*, 116780. [CrossRef]
33. Shields, Y.; Tsangouri, E.; Riordan, C.; De Nardi, C.; Assunção Godinho, G.R.; Ooms, T.; Antonaci, P.; Palmer, D.; Al-Tabbaa, A.; Jefferson, A.; et al. Non-destructive evaluation of ductile-porous versus brittle 3D printed vascular networks in self-healing concrete. *Cem. Concr. Comp.* **2024**, *145*, 105333. [CrossRef]
34. Friedrich, L.F.; Tanzi, B.N.R.; Colpo, A.B.; Sobczyk, M.; Lacidogna, G.; Niccolini, G.; Iturrioz, I. Analysis of Acoustic Emission Activity during Progressive Failure in Heterogeneous Materials: Experimental and Numerical Investigation. *Appl. Sci.* **2022**, *12*, 3918. [CrossRef]
35. Aldea, C.-M.; Song, W.-J.; Popovics, J.S.; Shah, S.P. Extent of Healing of Cracked Normal Strength Concrete. *J. Mater. Civ. Eng.* **2000**, *12*, 92–96. [CrossRef]
36. Ferrara, L.; Krelani, V.; Carsana, M. A "fracture testing" based approach to assess crack healing of concrete with and without crystalline admixtures. *Constr. Build. Mater.* **2014**, *68*, 535–551. [CrossRef]
37. Grosse, C.U.; Ohtsu, M.; Aggelis, D.G.; Shiotani, T. (Eds.) *Acoustic Emission Testing: Basics for Research–Applications in Engineering*; Springer International Publishing: Cham, Switzerland, 2022. [CrossRef]
38. Carpinteri, A.; Lacidogna, G.; Corrado, M.; Di Battista, E. Cracking and crackling in concrete-like materials: A dynamic energy balance. *Eng. Fract. Mech.* **2016**, *155*, 130–144. [CrossRef]
39. Iturrioz, I.; Lacidogna, G.; Carpinteri, A. Experimental analysis and truss-like discrete element model simulation of concrete specimens under uniaxial compression. *Eng. Fract. Mech.* **2013**, *110*, 81–98. [CrossRef]
40. Jefferson, T.; Javierre, E.; Freeman, B.; Zaoui, A.; Koenders, E.; Ferrara, L. Research Progress on Numerical Models for Self-Healing Cementitious Materials. *Adv. Mater. Interfaces* **2018**, *5*, 1701378. [CrossRef]
41. Schlangen, E.; Joseph, C. Modelling of Self-Healing Cementitious Materials. In *Self-Healing Phenomena in Cement-Based Materials*; De Rooij, M., Van Tittelboom, K., De Belie, N., Schlangen, E., Eds.; Springer Netherlands: Dordrecht, The Netherlands, 2013; Volume 11, pp. 217–240.
42. Needleman, A. A Continuum Model for Void Nucleation by Inclusion Debonding. *J. Appl. Mech.* **1987**, *54*, 525–531. [CrossRef]
43. Belytschko, T.; Chen, H.; Xu, J.; Zi, G. Dynamic crack propagation based on loss of hyperbolicity and a new discontinuous enrichment. *Int. J. Numer. Methods Eng.* **2003**, *58*, 1873–1905. [CrossRef]

44. Park, T.; Ahmed, B.; Voyiadjis, G.Z. A review of continuum damage and plasticity in concrete: Part I–Theoretical framework. *Int. J. Damage Mech.* **2022**, *31*, 901–954. [CrossRef]
45. Voyiadjis, G.Z.; Ahmed, B.; Park, T. A review of continuum damage and plasticity in concrete: Part II–Numerical framework. *Int. J. Damage Mech.* **2022**, *31*, 762–794. [CrossRef]
46. Ponnusami, S.A.; Krishnasamy, J.; Turteltaub, S.; Van Der Zwaag, S. A cohesive-zone crack healing model for self-healing materials. *Int. J. Solids Struct.* **2018**, *134*, 249–263. [CrossRef]
47. Freeman, B.L.; Jefferson, T. The simulation of transport processes in cementitious materials with embedded healing systems. *Int. J. Numer. Anal. Methods Geomech.* **2020**, *44*, 293–326. [CrossRef]
48. Freeman, B.L.; Bonilla-Villalba, P.; Mihai, I.C.; Alnaas, W.F.; Jefferson, A.D. A specialised finite element for simulating self-healing quasi-brittle materials. *Adv. Model. Simul. Eng. Sci.* **2020**, *7*, 32. [CrossRef]
49. Bobaru, F.; Foster, J.T.; Geubelle, P.H.; Silling, S.A. (Eds.) *Handbook of Peridynamic Modeling*; Chapman and Hall/CRC: Boca Raton, FL, USA, 2016. [CrossRef]
50. Chen, Z.; Peng, X.; Jafarzadeh, S.; Bobaru, F. Analytical solutions of peridynamic equations. Part II: Elastic wave propagation. *Int. J. Eng. Sci.* **2023**, *188*, 103866. [CrossRef]
51. Madenci, E.; Oterkus, E. *Peridynamic Theory and Its Applications*; Springer: New York, NY, USA, 2014; ISBN 978-1-4614-8464-6.
52. Ongaro, G.; Bertani, R.; Galvanetto, U.; Pontefisso, A.; Zaccariotto, M. A multiscale peridynamic framework for modelling mechanical properties of polymer-based nanocomposites. *Eng. Fract. Mech.* **2022**, *274*, 108751. [CrossRef]
53. Sheikhbahaei, P.; Mossaiby, F.; Shojaei, A. An efficient peridynamic framework based on the arc-length method for fracture modeling of brittle and quasi-brittle problems with snapping instabilities. *Comput. Math. Appl.* **2023**, *136*, 165–190. [CrossRef]
54. Shojaei, A.; Hermann, A.; Cyron, C.J.; Seleson, P.; Silling, S.A. A hybrid meshfree discretization to improve the numerical performance of peridynamic models. *Comput. Methods Appl. Mech. Eng.* **2022**, *391*, 114544. [CrossRef]
55. Shojaei, A.; Hermann, A.; Seleson, P.; Silling, S.A.; Rabczuk, T.; Cyron, C.J. Peridynamic elastic waves in two-dimensional unbounded domains: Construction of nonlocal Dirichlet-type absorbing boundary conditions. *Comput. Methods Appl. Mech. Eng.* **2023**, *407*, 115948. [CrossRef]
56. Silling, S.A.; Askari, E. A meshfree method based on the peridynamic model of solid mechanics. *Comput. Struct.* **2005**, *83*, 1526–1535. [CrossRef]
57. Hansen, A.; Hemmer, P.C.; Pradhan, S. (Eds.) *The Fiber Bundle Model: Modeling Failure in Materials*, 1st ed.; Wiley: Hoboken, NJ, USA, 2015. [CrossRef]
58. Daniels, H.E. The statistical theory of the strength of bundles of threads. I. *Proc. R. Soc. Lond. A* **1945**, *183*, 405–435. [CrossRef]
59. Alava, M.J.; Nukala, P.K.V.V.; Zapperi, S. Statistical Models of Fracture. *Adv. Phys.* **2006**, *55*, 349–476. [CrossRef]
60. Biswas, S.; Ray, P.; Chakrabarti, B.K. *Statistical Physics of Fracture, Breakdown, and Earthquake: Effects of Disorder and Heterogeneity*, 1st ed.; Wiley: Hoboken, NJ, USA, 2015; ISBN 978-3-527-41219-8.
61. De Arcangelis, L.; Redner, S.; Herrmann, H.J. A random fuse model for breaking processes. *J. Phyique Lett.* **1985**, *46*, 585–590. [CrossRef]
62. Rucka, M.; Knak, M.; Nitka, M. A study on microcrack monitoring in concrete: Discrete element method simulations of acoustic emission for non-destructive diagnostics. *Eng. Fract. Mech.* **2023**, *293*, 109718. [CrossRef]
63. Šavija, B.; Feiteira, J.; Araújo, M.; Chatrabhuti, S.; Raquez, J.-M.; Van Tittelboom, K.; Gruyaert, E.; De Belie, N.; Schlangen, E. Simulation-Aided Design of Tubular Polymeric Capsules for Self-Healing Concrete. *Materials* **2016**, *10*, 10. [CrossRef]
64. Lv, L.-Y.; Zhang, H.; Schlangen, E.; Yang, Z.; Xing, F. Experimental and numerical study of crack behaviour for capsule-based self-healing cementitious materials. *Constr. Build. Mater.* **2017**, *156*, 219–229. [CrossRef]
65. Rodríguez, C.R.; Figueiredo, S.C.; Deprez, M.; Snoeck, D.; Schlangen, E.; Šavija, B. Numerical investigation of crack self-sealing in cement-based composites with superabsorbent polymers. *Cem. Concr. Compos.* **2019**, *104*, 103395. [CrossRef]
66. Sayadi, S.; Chang, Z.; He, S.; Schlangen, E.; Mihai, I.C.; Jefferson, A. An enhanced lattice beam element model for the numerical simulation of rate-dependent self-healing in cementitious materials. *Eng. Fract. Mech.* **2023**, *292*, 109632. [CrossRef]
67. Cibelli, A.; Pathirage, M.; Cusatis, G.; Ferrara, L.; Di Luzio, G. A discrete numerical model for the effects of crack healing on the behaviour of ordinary plain concrete: Implementation, calibration, and validation. *Eng. Fract. Mech.* **2022**, *263*, 108266. [CrossRef]
68. Riera, J.D. Local effects in impact problems on concrete structures. In Proceedings of the Conference on Structural Analysis and Design of Nuclear Power Plants, Porto Alegre, Brazil, 3–5 October 1984; p. 412.
69. Rojo Tanzi, B.N.; Sobczyk, M.; Iturrioz, I.; Lacidogna, G. Damage Evolution in Quasi-Brittle Materials: Experimental Analysis by AE and Numerical Simulation. *Appl. Sci.* **2023**, *13*, 10947. [CrossRef]
70. Anglani, G.; Montanari, P.M.; Marc Tulliani, J.; Lacidogna, G.; Antonaci, P. Evaluation of the self-healing effect in cement-based materials with embedded cementitious capsules by means of Acoustic Emission techniques. *MATEC Web Conf.* **2023**, *378*, 04004. [CrossRef]
71. TECHNICAL DATA SHEET-CARBOSTOP U. (n.d.). Available online: https://www.minovaglobal.com/media/1663/carbostop-u-tds.pdf (accessed on 29 April 2024).

72. Anglani, G.; Tulliani, J.-M.; Antonaci, P. Behaviour of Pre-Cracked Self-Healing Cementitious Materials under Static and Cyclic Loading. *Materials* **2020**, *13*, 1149. [CrossRef] [PubMed]
73. Anglani, G.; Van Mullem, T.; Tulliani, J.M.; Van Tittelboom, K.; De Belie, N.; Antonaci, P. Durability of Self-Healing Cementitious Systems with Encapsulated Polyurethane Evaluated with a New Pre-Standard Test Method. *Mater. Struct. Constr.* **2022**, *55*, 143. [CrossRef]
74. Anglani, G.; Montanari, P.M.; Iturrioz, I.; Antonaci, P.; Lacidogna, G. Damage assessment and performance evaluation of self-repaired concrete specimens under constant amplitude, high-cycle fatigue. *Procedia Struct. Integr.* **2023**, *47*, 552–562. [CrossRef]
75. Tanzi, B.N.R.; Sobczyk, M.; Becker, T.; González, L.A.S.; Vantadori, S.; Iturrioz, I.; Lacidogna, G. Damage evolution analysis in a "spaghetti" bridge model using the acoustic emission technique. *Appl. Sci.* **2021**, *11*, 2718. [CrossRef]
76. ACOUSTIC EMISSION-AEMISSION. 2024. Available online: https://lunitek.it/seismic/acoustic-emission/aemission/ (accessed on 29 April 2024).
77. Birck, G.; Iturrioz, I.; Lacidogna, G.; Carpinteri, A. Damage process in heterogeneous materials analyzed by a lattice model simulation. *Eng. Fail. Anal.* **2016**, *70*, 157–176. [CrossRef]
78. Jenabidehkordi, A. Computational methods for fracture in rock: A review and recent advances. *Front. Struct. Civ. Eng.* **2019**, *13*, 273–287. [CrossRef]
79. Nayfeh, A.H.; Hefzy, M.S. Continuum modeling of three-dimensional truss-like space structures. *AIAA J.* **1978**, *16*, 779–787. [CrossRef]
80. Jivkov, A.P.; Yates, J.R. Elastic behaviour of a regular lattice for meso-scale modelling of solids. *Int. J. Solids Struct.* **2012**, *49*, 3089–3099. [CrossRef]
81. Hillerborg, A. *A Model for Fracture Analysis*; Division of Building Materials, LTH, Lund University: Lund, Sweden, 1978; Volume 3005.
82. Tanzi, B.N.R.; Birck, G.; Sobczyk, M.; Iturrioz, I.; Lacidogna, G. Truss-like Discrete Element Method Applied to Damage Process Simulation in Quasi-Brittle Materials. *Appl. Sci.* **2023**, *13*, 5119. [CrossRef]
83. Carpinteri, A. Application of Fracture Mechanics to Concrete Structures. *J. Struct. Div.* **1982**, *108*, 833–848. [CrossRef]
84. Kosteski, L.E.; Iturrioz, I.; Lacidogna, G.; Carpinteri, A. Size effect in heterogeneous materials analyzed through a lattice discrete element method approach. *Eng. Fract. Mech.* **2020**, *232*, 107041. [CrossRef]
85. Determination of the fracture energy of mortar and concrete by means of three-point bend tests on notched beams. *Mater. Struct.* **1985**, *18*, 287–290. [CrossRef]